MATERIALS CHEMISTRY FRONTIERS

CHINESE CHEMICAL SOCIETY

ROYAL SOCIETY OF CHEMISTRY

RESEARCH ARTICLE

View Article Online
View Journal | View Issue

Cite this: *Mater. Chem. Front.*, 2021, **5**, 4225

Nitrogen dopant induced highly selective CO_2 reduction over lotus-leaf shaped ZnO nanorods†

Fang Lü,‡[a] Haihong Bao,‡[a] Fei He,‡[b] Gaocan Qi,*[a] Jiaqiang Sun,[c] Shusheng Zhang,[d] Longchao Zhuo,[e] Hui Yang,*[a] Guangzhi Hu,[f] Jun Luo[a] and Xijun Liu*[ag]

Received 1st March 2021,
Accepted 25th March 2021

DOI: 10.1039/d1qm00344e

rsc.li/frontiers-materials

Heteroatom doping offers great promise for boosting the electrocatalytic activity for the CO_2 reduction reaction (CO_2RR). Herein, nitrogen-doped ZnO nanorods with a lotus-leaf shape were constructed as the active electrocatalysts, demonstrating enhanced CO_2RR performance with a maximum CO faradaic efficiency of 76% at −0.7 V (*vs.* reversible hydrogen electrode, RHE) and excellent durable activity of more than 30 h. Density functional calculations reveal that doping nitrogen in ZnO induced the reduction of free-energy barrier for the key intermediate (*COOH) formation and the enhancement of electron exchange, thereby leading to a notable improvement in the CO_2RR activity over these low-cost N-doped ZnO nanorods.

Introduction

The greenhouse effect due to CO_2 has seriously influenced the carbon cycle in nature and posed a severe threat to human life.[1,2] Electrocatalytic CO_2 reduction reaction (CO_2RR) is a promising technology that can convert CO_2 to valuable feedstocks and chemical fuels.[3–8] Thus far, great efforts have been devoted to searching for suitable materials for CO_2 electroreduction. Among these materials, transition metal electrocatalysts such as Co,[9] Ni,[10] Bi,[11] Cu,[12,13] Ag[14] and Zn[15,16] are ideal candidates for converting CO_2 to chemical fuels because their d bands contain valence electrons close to the Fermi level,[17] thus beneficial for overcoming the activation barriers of the reduction reaction.

In the past decades, earth-abundant and environmentally friendly Zn-based materials have attracted much attention as CO_2RR electrocatalysts due to their high adsorption affinity towards CO_2 molecules.[18,19] However, bulk Zn catalysts require large overpotentials with low reaction activity, due to fewer active sites.[20] To enhance the catalytic activity, significant efforts have focused on the structural design and morphology of Zn-based catalysts, including dendritic Zn,[21] hexagonal Zn,[22] nanoporous ZnO[23] and ZnO nanosheets.[24] Previous studies have confirmed heteroatom doping (such as B, N, P and S) to be an effective strategy for increasing the electrocatalytic activity. The introduction of dopants not only induces a great change in the electronic structure and enhances the conductivity, but also reduces the activation energy barrier of the electrocatalytic reaction.[25–27] Recently, we have developed a facile approach to dope nitrogen into Ti_3C_2 MXene nanosheets for electrocatalytic CO_2 reduction to produce CO.[28]

In this study, nitrogen-doped ZnO nanorods with lotus-leaf shape were fabricated as active electrocatalysts for CO_2 conversion using a facile hydrothermal growth and subsequent plasma treatment process. Compared with undoped ones, N-doped ZnO nanorods exhibited a significant improvement in CO generation with a maximum faradaic efficiency (FE_{CO}) of 76% at −0.7 V (*vs.* reversible hydrogen electrode, RHE) and excellent durable activity of more than 30 h. Theoretical calculations confirm that the introduction of nitrogen dopants is beneficial for reducing the activation barrier for the key intermediate (*COOH) formation and enhancing the electron exchange between N dopants and coordinated Zn atoms, resulting in an outstanding CO_2RR performance.

[a] *Tianjin Key Lab for Photoelectric Materials & Devices, School of Materials Science and Engineering, Tianjin University of Technology, Tianjin 300384, China. E-mail: xjliu@tjut.edu.cn, gaocanqi@tjut.edu.cn, y.hui1021@tjut.edu.cn*
[b] *Key Laboratory of Chemistry of Plant Resources in Arid Regions, State Key Laboratory Basis of Xinjiang Indigenous Medicinal Plants Resource Utilization, Xinjiang Technical Institute of Physics and Chemistry, Chinese Academy of Sciences, Urumqi, 830011, China*
[c] *State Key Laboratory of Coal Conversion, Institute of Coal Chemistry, Chinese Academy of Sciences, Taiyuan 030001, Shanxi, China*
[d] *College of Chemistry, Zhengzhou University, Zhengzhou 450000, China*
[e] *School of Materials Science and Engineering, Xi'an University of Technology, Xi'an 710048, Shanxi, China*
[f] *College of Biological, Chemical Sciences and Engineering, Jiaxing University, Jiaxing, Zhejiang 314001, China*
[g] *Key Laboratory of Civil Aviation Thermal Hazards Prevention and Emergency Response, Civil Aviation University of China, Tianjin, 300300, China*

† Electronic supplementary information (ESI) available. See DOI: 10.1039/d1qm00344e

‡ These authors contributed equally to this work.

Results and discussion

The N-doped ZnO nanorods were fabricated according to the previously reported method[29] and the schematic illustration is shown in Fig. 1a. ZnO nanorods were first grown on ITO conductive glass by the hydrothermal method, and the morphology of ZnO looks like lotus leaves as observed by scanning electron microscopy (SEM) (Fig. S1, ESI†). The N-doped ZnO nanorods were obtained by following the plasma treatment process, and these nanorods showed a similar morphology to that of lotus leaves in the undoped ones, represented in Fig. 1b (Fig. S2, ESI†) and transmission electron microscopy (TEM) (Fig. 1c) images. The corresponding high-resolution TEM (HRTEM) image (Fig. 1d) exhibits a lattice fringe distance of 0.26 nm, which corresponds to the (002) plane spacing of ZnO material. Additionally, N elements were distributed uniformly in the ZnO nanorods according to elemental mapping images from energy-dispersive X-ray spectroscopy (EDS) (Fig. 1e), and the content of nitrogen dopants in these N-doped ZnO nanorods was about 0.52 wt%.

The crystallographic structure was investigated by XRD patterns, (Fig. 2a) and all diffraction peaks for undoped and N-doped ZnO nanorods were approximately identical with no peak shifts, corresponding to the JCPDS files #75-1526 of ZnO. Nevertheless, the change in the surface chemical structure of N-doped ZnO nanorods was also measured by X-ray photoelectron spectroscopy (XPS) and is shown in Fig. 2. The binding energies of Zn $2p_{3/2}$ and Zn $2p_{1/2}$ peaks for N-doped ZnO nanorods are 1022.1 eV and 1045.1 eV, respectively. Obviously, the binding energy for Zn^{2+} showed a right shift of ~0.2 eV for N-doped ZnO nanorods compared to the undoped ones (Fig. 2b). This indicates that a part of electrons have been transferred away from Zn, which may be caused by the introduction of N after the plasma treatment. The O 1s spectrum shown in Fig. 2c exhibits a very broad peak and can be deconvoluted into three peaks at 530.6 eV, 531.6 eV and 532.6 eV, which were assigned to O^{2-} of lattice oxygen, deficient oxygen and chemically adsorbed oxygen, respectively.[30] The binding energy of N 1s peak in N-doped ZnO (Fig. 2d) also can be deconvoluted into two peaks at 397.6 eV and 399.4 eV, which were assigned to Zn–N[31] and O–N[32] species (~400 eV), indicating that N atoms have been successfully doped into ZnO nanorods.

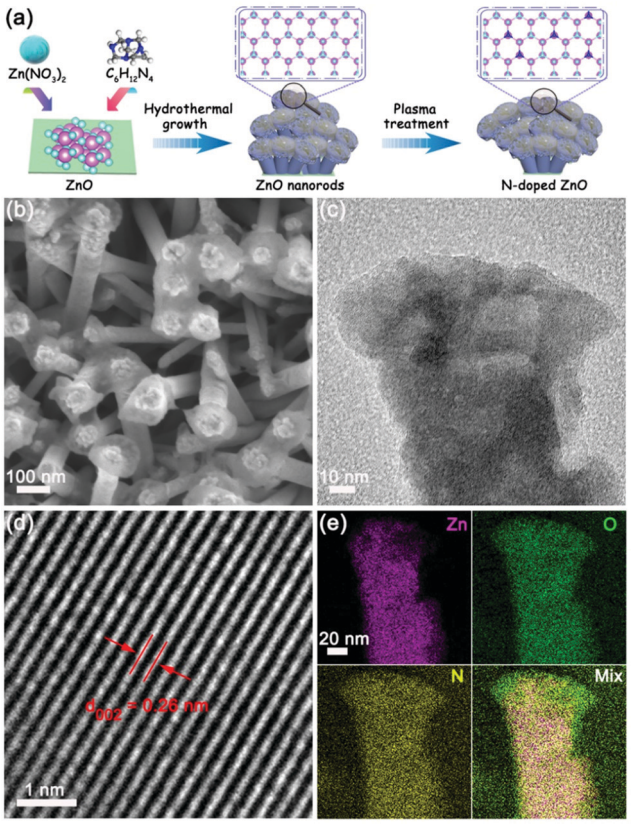

Fig. 1 (a) Schematic illustration of the preparation, (b) SEM image, (c) TEM image, (d) high-magnification TEM image, and (e) EDS elemental mapping images of N-doped ZnO nanorods.

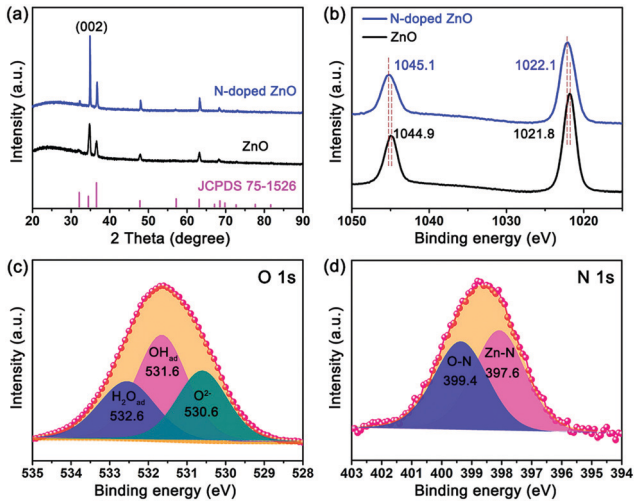

Fig. 2 The structural characterization of ZnO and N-doped ZnO nanorods. (a) XRD patterns, (b) XPS spectra of Zn 2p, XPS fitting spectra of (c) O 1s and (d) N 1s of N-doped ZnO.

The electrocatalytic CO_2 performance of the electrodes based on lotus leaf-shaped ZnO and N-doped ZnO nanorods were evaluated in a H-cell separated by a Nafion-115 proton exchange membrane with CO_2-saturated 0.5 M $KHCO_3$ (pH = 7.2), as previously reported by our group.[33] The linear sweep voltammetry (LSV) curves were obtained using 90% iR-offset to compensate the drop of ohmic potential caused by electrolyte resistance. All potentials were reported with respect to the RHE, and each current density was normalized by the geometric area of the electrode. From LSV curves (Fig. S3 and S4, ESI†), the N-doped ZnO electrode showed lower overpotential and higher current density under CO_2 atmosphere compared to N_2 atmosphere, indicating better electrocatalytic activity for CO_2RR. However, the undoped ZnO electrode showed lower current density under CO_2 atmosphere compared to N_2 (Ar) atmosphere, indicating better electrocatalytic activity for hydrogen evolution reaction. The N-doped ZnO electrode (Fig. 3a) exhibited a reduction current density of 5.6 mA cm^{-2} at −0.7 V *vs.* RHE; this value is 2.4 times greater than that of the undoped one,

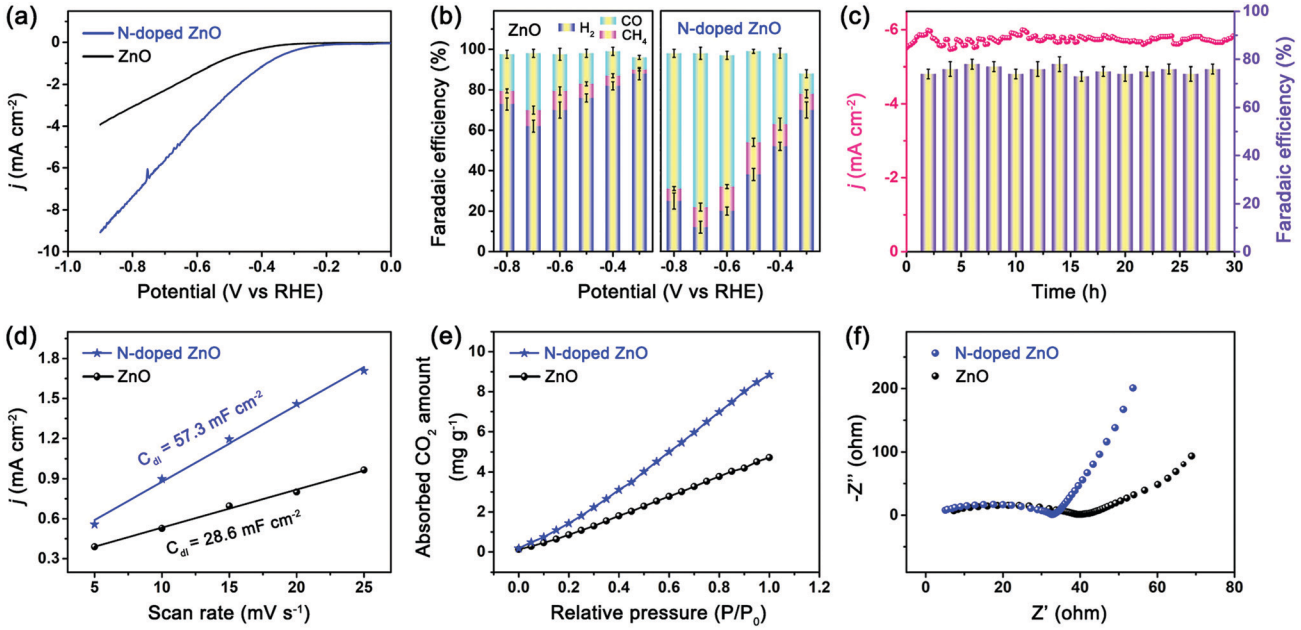

Fig. 3 The CO_2RR performance of ZnO and N-doped ZnO nanorods. (a) LSV curves, (b) FEs of CO, CH_4 and H_2 at various applied potentials, (c) stability test for N-doped ZnO nanorods at −0.7 V *vs.* RHE and the FE variation for CO production, (d) charging current density differences *j* plotted against the scan rates, (e) CO_2 adsorption isotherms, and (f) Nyquist plots of EIS.

indicating a higher catalytic activity over the N-doped ZnO nanorods as compared to the undoped counterpart.

The products were quantitatively analyzed by gas chromatography (GC) and ^{1}H nuclear magnetic resonance (NMR) spectrometry. Consequently, only CO, H_2 and CH_4 were detected and no liquid products were observed. The NMR spectrum of the N-doped ZnO electrode for CO_2RR recorded at −0.7 V *vs.* RHE is shown in Fig. S5 (ESI†). The dependence of faradaic efficiency (FE) for different products on the applied potentials for both electrodes is shown in Fig. 3b. At a low applied potential of −0.3 V *vs.* RHE, low FE values for CO (11 ± 4%) and CH_4 (7 ± 4%) production were observed over the N-doped ZnO electrode, while H_2 (70 ± 4%) was the dominant product. With further increase in the applied potential, a maximum FE_{CO} of 76 ± 4% was achieved at −0.7 V *vs.* RHE, as well as a small amount of CH_4 (∼8%) and H_2 (∼14%) were detected. For observed products, the sum of FEs was above 90.0% for the syngas with a ratio of CO/H_2 of 5.4, and also generates controllable ratios of syngas with varying potential during the CO_2RR. For the reference ZnO electrode, the hydrogen evolution reaction (HER) dominated the entire potential in the range from −0.3 to −0.8 V *vs.* RHE, and it showed a maximum FE_{CO} of 28% at −0.7 V *vs.* RHE, indicating low activity for reducing CO_2 to CO.

The long-term stability of electrocatalysts is another crucial indicator in evaluating the CO_2 reduction performance. The current density of N-doped ZnO electrode was relatively stable with a value of 5.6 mA cm^{-2} at −0.7 V *vs.* RHE even after 30 h (Fig. 3c). Notably, the corresponding FE for CO production was constantly maintained to be greater than 75% for a duration of 30 h. Meanwhile, the structure and morphology of the N-doped ZnO after CO_2RR are shown in Fig. S6 (ESI†). Also, the corresponding Nyquist plot after the long-term electrolysis of the N-doped ZnO electrode has been obtained and is shown in Fig. S7 (ESI†). After long-term electrolysis, the plot exhibited a little larger semicircle than before CO_2 reduction, which indicates a higher interfacial charge-transfer resistance and a little decrease in the conductivity. The observed results showed that the N-doped ZnO nanorods showed a good structural and electrochemical stability.

The electrochemically active surface area of the electrodes was determined by double-layer capacitance (C_{dl}) to investigate the underlying kinetic mechanism for the enhanced CO_2RR performance. The measured C_{dl} of the N-doped ZnO nanorods was 57.3 mF cm^{-2}, approximately double that of the undoped counterpart (28.6 mF cm^{-2}), which confirms an increased number of catalytically active sites because of N doping and subsequently improved electroreduction activity. Furthermore, the volumetric CO_2 adsorption isotherms showed that N-doped ZnO nanorods exhibited much higher CO_2 adsorption capacity (10.3 cm^3 g^{-1}) compared to that of the undoped counterpart, confirming that N-doped ZnO nanorods have much more abundant adsorption sites for CO_2 on the surface due to the doping of nitrogen. The charge-transfer resistance values at the interfaces for the two electrodes were obtained by electrochemical impedance spectroscopy (EIS). The Nyquist plot of N-doped ZnO nanorods exhibited a much smaller semicircle and a steeper slope, which indicated a lower interfacial charge-transfer resistance and better conductivity, suggesting a much faster faradaic process. The Tafel plots (Fig. S8, ESI†) show that in the linear Tafel region, N-doped ZnO nanorods exhibited a lower Tafel slope (169 mV dec^{-1}) than undoped ZnO nanorods (192 mV dec^{-1}), indicating that the single-electron transfer to

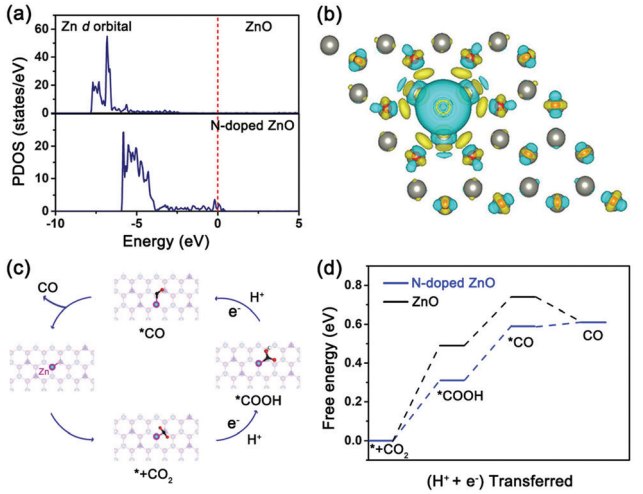

Fig. 4 DFT calculations. (a) Calculated PDOS of Zn *d*-orbital in N-doped and undoped ZnO nanorods, (b) differential charge diagram of ZnO with nitrogen dopant, the gray, red, and white spheres represent Zn, O, and N atoms, respectively. (c) A possible reaction path for CO_2RR to CO on N-doped ZnO nanorods, and (d) DFT free energy profiles of CO_2RR to CO.

CO_2 is the rate-determining step for CO_2 reduction to CO[34] on the two ZnO electrodes, and N-doping of ZnO improved the CO_2 reduction thermodynamic kinetics, which is consistent with the LSV analysis (Fig. 3a).

To further provide a theoretical insight into the underlying mechanism, we performed DFT calculations to calculate the density of states, differential charge density and the Gibbs free energy of the two nanorods. The projected density of states (PDOS) of Zn *d*-orbitals in the two nanorods are presented in Fig. 4a. N-Doped ZnO exhibits a significant increase in the density of states near the Fermi level compared to the undoped counterpart, which can enhance the electron exchange with the reactants and intermediates during the reaction of Zn atoms, thus improving the reactivity of CO_2 electroreduction.[35] The differential charge density of O–N–Zn in N-doped ZnO (Fig. 4b) revealed that the charge between N and active Zn atoms was accumulated, and the electron exchange between the N dopants and coordinated Zn atoms was much easier than that between the O and Zn atoms.

On the basis of above results and Tafel values, a possible mechanism for CO_2 electroreduction to CO over N-doped ZnO (Fig. 4c) was proposed, where the overall path proceeds as $CO_2 \rightarrow *CO_2 \rightarrow *COOH \rightarrow *CO \rightarrow CO$, which is in agreement with the previous reports.[19,36] Initially, a CO_2 molecule gets adsorbed on the N site of ZnO surface and then generates $*CO_2$. After that, the adsorbed $*CO_2$ couples with a proton from the electrolyte to form *COOH intermediate, and this step is identified as the rate-limiting step (RLS). Finally, the *COOH intermediate leaves off the $H^+ + e^-$ reactants to form H_2O product and produce CO. DFT calculations were performed to gain the reaction free energy profile (Fig. 4d) and to analyze the kinetics of elementary steps in the CO_2RR catalyzed by these two samples. It can be clearly seen that the activation energy barrier of the *COOH intermediate for N-doped ZnO (0.31 eV) is much lower than that of undoped ZnO (0.49 eV). Owing to the difference of 0.18 eV in activation barrier, the *COOH intermediate formation is much easier over N-doped ZnO and further promotes CO formation at lower overpotentials. Therefore, the reduction of the free-energy barrier and the enhanced electron exchange induced by N dopants provide superior CO_2RR performance for N-doped ZnO nanorods with a lotus-leaf shape.

Conclusion

In summary, N-doped ZnO nanorods with a lotus-leaf shape were prepared by a simple hydrothermal synthesis and plasma treatment method. It exhibited an enhanced CO_2RR performance with a maximum CO faradaic efficiency of 76% at −0.7 V *vs.* RHE. Further, more than 30 h durability test confirmed its excellent stability for the CO_2RR. Theoretical calculations revealed that the nitrogen dopants enhance the electron exchange between the N dopants and coordinated Zn atoms, which induces the reduction of free-energy barriers and thus facilitates the formation of the intermediate (*COOH). Finally, these N-doped ZnO nanorods with a lotus-leaf shape show superb CO_2RR activity.

Author contributions

Xijun Liu, Hui Yang and Gaocan Qi designed the catalyst; Fang Lü, Haihong Bao and Fei He performed the experiments and DFT calculations; Jiaqiang Sun, Shusheng Zhang, Longchao Zhuo, and Jun Luo co-analyzed data; Gaocan Qi and Hui Yang co-wrote the manuscript; Xijun Liu revised the manuscript. All the authors discussed and commented on the data and contributed to the manuscript.

Conflicts of interest

There are no conflicts to declare.

Acknowledgements

This work was financially supported by National Natural Science Foundation of China (22075211, 21601136, 21501132, 51971157, 12074017 and 51621003), Tianjin Science Fund for Distinguished Young Scholars (19JCJQJC61800), the Science and Technology Development Fund of Tianjin Education Commission for Higher Education (2018KJ126) and Tianjin Natural Science Foundation (18JCQNJC77100). The authors acknowledge Beijng PARATERA Tech Co., Ltd for providing HPC resources that have contributed to the research results reported within this paper.

References

1 B. A. Rosen, A. Salehi-Khojin, M. R. Thorson, W. Zhu, D. T. Whipple, P. J. A. Kenis and R. I. Masel, Ionic liquid-mediated selective conversion of CO to CO at low overpotentials, *Science*, 2011, **334**, 643.

2 Y. Zheng, A. Vasileff, X. Zhou, Y. Jiao, M. Jaroniec and S. Z. Qiao, Understanding the roadmap for electrochemical reduction of CO_2 to multi-carbon oxygenates and hydrocarbons on copper-based catalysts, *J. Am. Chem. Soc.*, 2019, **141**, 7646–7659.
3 X. Liu, H. Yang, J. He, H. Liu, L. Song, L. Li and J. Luo, Highly active, durable ultrathin $MoTe_2$ layers for the electroreduction of CO_2 to CH_4, *Small*, 2018, **14**, 1704049.
4 J. Zhu, J. Fan, T. Cheng, M. Cao, Z. Sun, R. Zhou, L. Huang, D. Wang, Y. Li and Y. Wu, Bilayer nanosheets of unusual stoichiometric bismuth oxychloride for potassium ion storage and CO_2 reduction, *Nano Energy*, 2020, **75**, 104939.
5 F. Lü, H. Bao, Y. Mi, Y. Liu, J. Sun, X. Peng, Y. Qiu, L. Zhuo, X. Liu and J. Luo, Electrochemical CO_2 reduction: from nanoclusters to single atom catalysts, *Sustainable Energy Fuels*, 2020, **4**, 1012–1028.
6 N. Han, P. Ding, L. He, Y. Li and Y. Li, Promises of main group metal–based nanostructured materials for electrochemical CO_2 reduction to formate, *Adv. Energy Mater.*, 2020, **10**, 1902338.
7 W. Wang, L. Shang, G. Chang, C. Yan, R. Shi, Y. Zhao, G. I. N. Waterhouse, D. Yang and T. Zhang, Intrinsic carbon-defect-driven electrocatalytic reduction of carbon dioxide, *Adv. Mater.*, 2019, **31**, 1808276.
8 P. Ding, H. Zhao, T. Li, Y. Luo, G. Chen, S. Gao, X. Shi, S. Lu and X. Sun, Metal-based electrocatalytic conversion of CO_2 to formic acid/formate, *J. Mater. Chem. A*, 2020, **8**, 21947–21960.
9 C. Liu, T. R. Cundari and A. K. Wilson, CO_2 reduction on transition metal (Fe, Co, Ni, and Cu) surfaces: in comparison with homogeneous catalysis, *J. Phys. Chem. C*, 2012, **116**, 5681–5688.
10 J. Yang, Z. Qiu, C. Zhao, W. Wei, W. Chen, Z. Li, Y. Qu, J. Dong, J. Luo, Z. Li and Y. Wu, In situ thermal atomization to convert supported nickel nanoparticles into surface-bound nickel single-atom catalysts, *Angew. Chem. Int. Ed.*, 2018, **57**, 14095–14100.
11 J. Yang, X. Wang, Y. Qu, X. Wang, H. Huo, Q. Fan, J. Wang, L. Yang and Y. Wu, Bi-based metal-organic framework derived leafy bismuth nanosheets for carbon dioxide electroreduction, *Adv. Energy Mater.*, 2020, **10**, 2001709.
12 A. Guan, Z. Chen, Y. Quan, C. Peng, Z. Wang, T. Sham, C. Yang, Y. Ji, L. Qian, X. Xu and G. Zheng, Boosting CO_2 electroreduction to CH_4 via tuning neighboring single-copper sites, *ACS Energy Lett.*, 2020, **5**, 1044–1053.
13 S. Shen, J. He, X. Peng, W. Xi, L. Zhang, D. Xi, L. Wang, X. Liu and J. Luo, Stepped surface-rich copper fiber felt as an efficient electrocatalyst for the CO_2RR to formate, *J. Mater. Chem. A*, 2018, **6**, 18960.
14 N. Zhang, X. Zhang, L. Tao, P. Jiang, C. Ye, R. Lin, Z. Huang, A. Li, D. Pang, H. Yan, Y. Wang, P. Xu, S. An, Q. Zhang, L. Liu, S. Du, X. Han, D. Wang and Y. Li, Silver single-atom catalyst for efficient electrochemical CO_2 reduction synthesized from thermal transformation and surface reconstruction, *Angew. Chem. Int. Ed.*, 2021, **60**, 6170–6176.
15 L. Han, S. Song, M. Liu, S. Yao, Z. Liang, H. Cheng, Z. Ren, W. Liu, R. Lin, G. Qi, X. Liu, Q. Wu, J. Luo and H. L. Xin, Stable and efficient single-atom Zn catalyst for CO_2 reduction to CH_4, *J. Am. Chem. Soc.*, 2020, **142**, 12563.
16 B. Qin, Y. Li, H. Fu, H. Wang, S. Chen, Z. Liu and F. Peng, Electrochemical reduction of CO_2 into tunable syngas production by regulating crystal facets of earth-abundant Zn catalyst, *ACS Appl. Mater. Inter.*, 2018, **10**, 20530–20539.
17 J. K. Nørskov, F. Abild-Pedersena, F. Studt and T. Bligaard, Density functional theory in surface chemistry and catalysis, *Proc. Natl. Acad. Sci. U. S. A.*, 2011, **108**, 937–943.
18 Q. Tang and Q. Luo, Adsorption of CO_2 at ZnO: A surface structure effect from DFT+U calculations, *J. Phys. Chem. C*, 2013, **117**, 22954–22966.
19 T. Zhang, X. Li, Y. Qiu, P. Su, W. Xu, H. Zhong and H. Zhang, Multilayered Zn nanosheets as an electrocatalyst for efficient electrochemical reduction of CO_2, *J. Catal.*, 2018, **357**, 154–162.
20 Y. Hori, H. Wakebe, T. Tsukamoto and O. Koga, Electrocatalytic process of CO selectivity in electrochemical reduction of CO_2 at metal electrodes in aqueous media, *Electrochim. Acta*, 1994, **39**, 1833–1839.
21 J. Rosen, G. S. Hutchings, Q. Lu, R. V. Forest, A. Moore and F. Jiao, Electrodeposited Zn dendrites with enhanced CO selectivity for electrocatalytic CO_2 reduction, *ACS Catal.*, 2015, **5**, 4586–4591.
22 D. H. Won, H. Shin, J. Koh, J. Chung, H. S. Lee, H. Kim and S. I. Woo, Highly efficient, selective, and stable CO_2 electroreduction on a hexagonal Zn catalyst, *Angew. Chem. Int. Ed.*, 2016, **55**, 9297–9300.
23 X. Jiang, F. Cai, D. Gao, J. Dong, S. Miao, G. Wang and X. Bao, Electrocatalytic reduction of carbon dioxide over reduced nanoporous zinc oxide, *Electrochem. Commun.*, 2016, **68**, 67–70.
24 Z. Geng, X. Kong, W. Chen, H. Su, Y. Liu, F. Cai, G. Wang and J. Zeng, Oxygen vacancies in ZnO nanosheets enhance CO_2 electrochemical reduction to CO, *Angew. Chem. Int. Ed.*, 2018, **57**, 6054–6059.
25 Y. Liu, S. Chen, X. Quan and H. Yu, Efficient electrochemical reduction of carbon dioxide to acetate on nitrogen-doped nanodiamond, *J. Am. Chem. Soc.*, 2015, **137**, 11631–11636.
26 C. Jia, W. Ren, X. Chen, W. Yang and C. Zhao, N, B) Dual heteroatom-doped hierarchical porous carbon framework for efficient electroreduction of carbon dioxide, *ACS Sustainable Chem. Eng.*, 2020, **8**, 6003–6010.
27 M. Kuang, A. Guan, Z. Gu, P. Han, L. Qian and G. Zheng, Enhanced N-doping in mesoporous carbon for efficient electrocatalytic CO_2 conversion, *Nano Res.*, 2019, **12**, 2324–2329.
28 D. Qu, X. Peng, Y. Mi, H. Bao, S. Zhao, X. Liu and J. Luo, Nitrogen-doping and titanium vacancies synergistically promote CO_2 fixation in seawater, *Nanoscale*, 2020, **12**, 17191.
29 G. Qi, S. Zhao and Z. Yuan, From function-guided assembly of a lotus leaf-like ZnO nanostructure to a formaldehyde gas-sensing application, *Sens. Actuators B-Chem.*, 2013, **184**, 143–149.
30 M. Chen, Z. Wang, D. Han, F. Gu and G. Guo, Porous ZnO polygonal nanoflakes: synthesis, use in high-sensitivity NO_2

gas sensor, and proposed mechanism of gas sensing, *Sens. Actuators B-Chem.*, 2011, **157**, 565–574.

31 C. L. Perkins, S. Lee, X. Li, S. E. Asher and T. J. Coutts, Identification of nitrogen chemical states in N-doped ZnO via x-ray photoelectron spectroscopy, *J. Appl. Phys.*, 2005, **97**, 034907.

32 J. A. Rengifo-Herrera, K. Pierzchala, A. Sienkiewicz, L. Forró, J. Kiwi, J. E. Moser and C. Pulgarin, Synthesis, characterization, and photocatalytic activities of nanoparticulate N, S-codoped TiO_2 having different surface-to-volume ratios, *J. Phys. Chem. C*, 2010, **114**, 2717–2723.

33 J. Fu, H. Bao, Y. Liu, Y. Mi, Y. Qiu, L. Zhuo, X. Liu and J. Luo, Oxygen doping induced by nitrogen vacancies in Nb_4N_5 enables highly selective CO_2 reduction, *Small*, 2020, **16**, 1905825.

34 Y. C. Hsieh, S. D. Senanayake, Y. Zhang, W. Xu and D. E. Polyansky, Effect of chloride anions on the synthesis and enhanced catalytic activity of silver nanocoral electrodes for CO_2 electroreduction, *ACS Catal.*, 2015, **5**, 5349–5356.

35 S. Zhao, Y. Wen, X. Peng, Y. Mi, X. Liu, Y. Liu, L. Zhuo, G. Hu, J. Luo and X. Tang, Isolated single-atom Pt sites for highly selective electrocatalytic hydrogenation of formaldehyde to methanol, *J. Mater. Chem. A*, 2020, **8**, 8913–8919.

36 S. Gao, Y. Lin, X. Jiao, Y. Sun, Q. Luo, W. Zhang, D. Li, J. Yang and Y. Xie, Partially oxidized atomic cobalt layers for carbon dioxide electroreduction to liquid fuel, *Nature*, 2016, **529**, 68–71.

